ELSEVIER

J. Non-Newtonian Fluid Mech. 91 (2000) 255–271

Journal of Non-Newtonian Fluid Mechanics

www.elsevier.com/locate/jnnfm

Emergence of structure in a model of liquid crystalline polymers with elastic coupling

Raz Kupferman [a], Mark N. Kawaguchi [b,c,1], Morton M. Denn [b,c,*]

[a] *Institute of Mathematics, The Hebrew University, Jerusalem 91904, Israel*

[b] *Materials Sciences Division, Lawrence Berkeley National Laboratory, Berkeley, CA 94720, USA*

[c] *Department of Chemical Engineering, University of California, Berkeley, CA 94720-1462, USA*

Received 11 August 1999

Abstract

We have solved the equations of transient shear flow for a model of a liquid crystalline polymer that contains a long-range interaction term in the nematic potential. The model exhibits a rich set of dynamics when the structure and momentum equations are coupled, including a periodic vorticity 'burst' near the shearing surface and very large gradients in velocity at discrete planes. Textures that are independent of the macroscopic scale were not observed.

Keywords: Liquid crystalline polymers; Elastic coupling

1. Introduction

Liquid crystalline polymers are inherently anisotropic. At rest, concentrated solutions and melts exhibit orientational texture, in which there is a local preferred orientation that extends over distances of order micrometers, but the sample is isotropic on a macroscopic scale; the texture is related to local orientational defects and is sometimes described as consisting of 'domains'. The texture evolves with shear and seems to vanish at high shear rates, but a texture always returns when the flow stresses have relaxed. Existing theories of anisotropic liquids predict the evolution of orientational structure in shear flow (some recent results, with references to the prior literature, can be found in [1] and [2]); the calculated textures are unlike those seen in liquid crystalline polymers, however, where the length scale of the texture appears to be independent of the macroscopic scale of the experimental equipment.

* Corresponding author. Present address: The Levich Institute, City College of the City University of New York, 1-M Steinman Hall, 140th Street at Convent Avenue, New York, NY 10031, USA. Fax.: +1-212-650-6835.

E-mail address: denn@levdec-engr.ccyy.cuny.edu (M.M. Denn)

[1] Present address: Applied Materials, 974 E Arques Ave., M/S 81330, Sunnyvale, CA 94086, USA.

0377-0257/00/$ – see front matter
PII: S0377-0257(99)00098-1

It is generally believed that long-range interactions (elastic coupling) must be included in the nematic potential to generate a constitutive theory of liquid crystalline polymers that can accommodate defect textures. The first such proposal seems to be by Marrucci and Greco [3]. Rey and Tsuji [4] have recently reported results for a 'complete' theory that includes long-range elastic interactions, and they show the evolution of defects in a quiescent system during the isotropic-nematic phase transition and the suppression of defect nucleation by shear. Their transient solution for shear flow was carried out without coupling between the orientation and momentum equations.

We report here on a fully-coupled transient simulation of shear flow for a model liquid that includes a long-range term in the potential, following Marrucci and Greco [3]. Quadratic closure is used to obtain a constitutive equation in closed form, and the finite aspect ratio of the underlying molecular rigid rod is retained in the formulation.

2. The model

Our model builds upon the original Doi theory [5,6], whose starting point is a Smoluchowski equation for the orientational distribution of molecules,

$$\frac{\partial \psi}{\partial t} = \nabla_u \cdot D_{\mathrm{R}} \left(\nabla_u \psi + \frac{\psi}{k_{\mathrm{B}} T} \nabla_u \varphi \right) - \nabla_u \cdot (\dot{\boldsymbol{u}} \psi) - \nabla \cdot (\boldsymbol{v} \psi), \tag{1}$$

where $\psi(\boldsymbol{u}, \boldsymbol{R}, t)$ is the probability of finding a molecular rod in an orientation $\boldsymbol{u}$ at a position $\boldsymbol{R}$ at time t. It is assumed that the molecules are rigid and uniaxial so that the molecular orientation is completely specified by the unit vector $\boldsymbol{u}$. The right-hand side of Eq. (1) represents the various forces that act upon a molecule: Brownian forces, represented by the first term, act to randomize the orientation with a characteristic rotational diffusion coefficient D_{R}, which, in general, depends on the orientational distribution ψ. A mean-field potential φ accounts for interactions between molecules, as well as external interactions, such as magnetic or electric fields, with k_{B} the Boltzmann constant and T the absolute temperature. Macroscopic flow affects the distribution through the rate of change of the molecular orientation $\dot{\boldsymbol{u}}$, while the third term accounts for the advection of the fluid by the macroscopic velocity field, $\boldsymbol{v}$. Translational diffusion was neglected here; such omission would be drastic if translational diffusion were the only spatial coupling in the model, but this is not the case if elastic coupling is taken into account. Two types of derivatives appear in (1): the orientational gradient, $\nabla_u = \partial/(\partial \boldsymbol{u})$, and the spatial gradient, $\nabla = \partial/(\partial \boldsymbol{R})$.

If the molecule is modeled as a rigid ellipsoid, the rate of change of its orientation is given by [7]

$$\dot{\boldsymbol{u}} = \boldsymbol{\omega} \cdot \boldsymbol{u} + \lambda(\boldsymbol{D} \cdot \boldsymbol{u} - \boldsymbol{D} : \boldsymbol{uuu}), \tag{2}$$

where products of vectors such as $\boldsymbol{uu}$ denote dyadic products, $\boldsymbol{\omega}$ and $\boldsymbol{D}$ are the vorticity and the rate-of-deformation tensors, respectively,

$$\boldsymbol{\omega} = \tfrac{1}{2}(\nabla \boldsymbol{v}^{\dagger} - \nabla \boldsymbol{v}), \tag{3}$$

$$\boldsymbol{D} = \tfrac{1}{2}(\nabla \boldsymbol{v}^{\dagger} + \nabla \boldsymbol{v}), \tag{4}$$

and the parameter λ is related to the molecular aspect ratio. For an infinite aspect ratio molecule, $\lambda \to 1$, in which case Eq. (2) reduces to the original expression proposed by Doi [5]. The finite-aspect ratio

description has appeared previously in studies of fiber suspensions (e.g., [8]), as well as in the work of Kuzuu and Doi [9,10].

The difficulty with microscopic models such as Eq. (1) is the high dimensionality of the governing equation, which makes it very hard to solve, even for the relatively simple case of spatially homogeneous solutions. Thus, the model requires substantial simplification before it is amenable to a tractable formulation.

A first common approximation is the replacement of the rotational diffusion coefficient D_R by a constant $\bar{D}_R$ that is independent of the local structure. Next, one derives an equation for the structure tensor $\boldsymbol{S}$ by multiplying Eq. (1) by the tensor $(\boldsymbol{uu}-(1/d)\boldsymbol{\delta})$ and integrating over all possible orientations [5,6] to obtain

$$\frac{\partial \boldsymbol{S}}{\partial t} = -2d\bar{D}_R\boldsymbol{S} - \frac{\bar{D}_R}{k_BT}[\langle \boldsymbol{u}(\boldsymbol{\nabla}_u\varphi)\rangle] + \langle(\boldsymbol{\nabla}_u\varphi)\boldsymbol{u}\rangle) + \frac{1}{d}(\boldsymbol{\kappa}+\boldsymbol{\kappa}^{\dagger}) + \boldsymbol{\kappa}\cdot\boldsymbol{S} + \boldsymbol{S}\cdot\boldsymbol{\kappa} \\ -2\boldsymbol{\kappa} : \langle \boldsymbol{uuuu}\rangle - \boldsymbol{v}\cdot\boldsymbol{\nabla}\boldsymbol{S}, \tag{5}$$

with

$$\boldsymbol{\kappa} = \boldsymbol{\omega} + \lambda\boldsymbol{D}. \tag{6}$$

d is the dimension of space.

In the present paper external fields are ignored, and we focus on the inter-molecular potential. Marrucci and Greco [3] proposed a mean-field potential of the following form:

$$\varphi = -2Uk_BT\left\{\boldsymbol{S} + \tfrac{1}{24}[R^2\nabla^2\boldsymbol{S} + L^2(\boldsymbol{uu} : \boldsymbol{\nabla\nabla})]\boldsymbol{S}\right\} : \boldsymbol{uu}. \tag{7}$$

The first term is the classical Maier–Saupe potential, the second arises from a spatially dependent potential between molecules with a characteristic interaction distance R, and the third represents a spatially dependent potential related to the length of the molecule, L. We will assume that the spatial interaction distance, R, is much larger than the molecular length, L, and neglect the inhomogeneous terms associated with the shape of the molecule; this is equivalent to taking the three Frank elastic constants to be equal. The parameter U is the nematic strength, or a dimensionless molecular concentration.

Substituting the potential (7) into the kinetic Eq. (5) gives rise to higher order moments, which must be approximated in order to close the system of equations. For both the interaction potential and flow terms, we use the quadratic closure approximation, namely

$$\boldsymbol{\kappa} : \langle \boldsymbol{uuuu}\rangle = \boldsymbol{\kappa} : \langle \boldsymbol{uu}\rangle\langle \boldsymbol{uu}\rangle, \quad \boldsymbol{S} : \langle \boldsymbol{uuuu}\rangle = \boldsymbol{S} : \langle \boldsymbol{uu}\rangle\langle \boldsymbol{uu}\rangle, \quad (\nabla^2\boldsymbol{S}) : \langle \boldsymbol{uuuu}\rangle = (\nabla^2\boldsymbol{S}) : \langle \boldsymbol{uu}\rangle\langle \boldsymbol{uu}\rangle. \tag{8}$$

Eq. (5) reduces then to a closed form, which we group following Doi [5]:

$$\left(\frac{\partial}{\partial t} + \boldsymbol{v}\cdot\boldsymbol{\nabla}\right)\boldsymbol{S} = \boldsymbol{F}(\boldsymbol{S}) + \boldsymbol{G}(\boldsymbol{S}). \tag{9}$$

The first term, $\boldsymbol{F}(\boldsymbol{S})$, represents the inter-molecular kinetics, which are subdivided into homogeneous and non-homogeneous terms,

$$\boldsymbol{F}(\boldsymbol{S}) = \boldsymbol{F}^{h}(\boldsymbol{S}) + \boldsymbol{F}^{nh}(\boldsymbol{S}), \tag{10}$$

with

$$\boldsymbol{F}^{h}(\boldsymbol{S}) = -2\bar{D}_R\boldsymbol{S} + 6\bar{D}_RU\left[\boldsymbol{S}\cdot\boldsymbol{S} + \tfrac{1}{d}\boldsymbol{S} - (\boldsymbol{S} : \boldsymbol{S})\boldsymbol{S} - \tfrac{1}{d}(\boldsymbol{S} : \boldsymbol{S})\boldsymbol{\delta}\right], \tag{11}$$

and

$$\boldsymbol{F}^{\mathrm{nh}}(\boldsymbol{S}) = \frac{\bar{D}_{\mathrm{R}}U}{8}R^2\left\{(\nabla^2\boldsymbol{S})\cdot\boldsymbol{S} + \boldsymbol{S}\cdot(\nabla^2\boldsymbol{S}) + \frac{2}{d}(\nabla^2\boldsymbol{S}) - 2[(\nabla^2\boldsymbol{S}):\boldsymbol{S}]\left(\boldsymbol{S}+\frac{1}{d}\boldsymbol{\delta}\right)\right\}. \tag{12}$$

The second term, $\boldsymbol{G}(\boldsymbol{S})$, represents the molecular advection terms:

$$\boldsymbol{G}(\boldsymbol{S}) = \tfrac{1}{d}(\boldsymbol{\kappa}+\boldsymbol{\kappa}^{\dagger}) + \boldsymbol{S}\cdot\boldsymbol{\kappa}^{\dagger} + \boldsymbol{\kappa}\cdot\boldsymbol{S} - 2(\boldsymbol{\kappa}:\boldsymbol{S})\left(\boldsymbol{S}+\tfrac{1}{d}\boldsymbol{\delta}\right). \tag{13}$$

Under macroscopic flow, the evolution Eq. (9) couples to the Cauchy momentum equation through the stress tensor. Accounting for the effects of the molecular aspect ratio and the spatially inhomogeneous interaction potential, via the virtual work approach used by Doi [5,6], results in the following expression for the elastic stress $\boldsymbol{\tau}^{\mathrm{e}}$:

$$\boldsymbol{\tau}^{\mathrm{e}} = -\frac{ck_{\mathrm{B}}T}{2\bar{D}_{\mathrm{R}}}\lambda\boldsymbol{F}(\boldsymbol{S}) + \frac{ck_{\mathrm{B}}TU}{16}R^2[(\nabla^2\boldsymbol{S})\cdot\boldsymbol{S} - \boldsymbol{S}\cdot(\nabla^2\boldsymbol{S})]. \tag{14}$$

In addition, the solvent contributes a viscous stress:

$$\boldsymbol{\tau}^{\mathrm{v}} = \eta_{\mathrm{s}}\boldsymbol{D}, \tag{15}$$

where η_{s} is the viscosity. (There is an additional stress term due to hydrodynamic drag caused by rod–rod friction which we neglect [11].) To within an isotropic pressure term, the stress tensor is given by the sum of the elastic and viscous components:

$$\boldsymbol{\tau} = \boldsymbol{\tau}^{\mathrm{e}} + \boldsymbol{\tau}^{\mathrm{v}}. \tag{16}$$

Eqs. (9)–(15) specify our constitutive model. Several points should be noticed: (i) Even though the literature has associated the quadratic closure approximation with a loss of periodic solutions, it can be shown that the incorporation of a finite aspect ratio with quadratic closure maintains periodic solutions such as tumbling, wagging, log-rolling, and kayaking [11]. (ii) One of the homogeneous models proposed by Feng and co-workers [2] differs from our homogeneous component by a factor of λ for the elastic stress tensor. (iii) Note that spatial inhomogeneities break the symmetry of the stress tensor (14), implying that torques generated within the material can propagate. The asymmetry of the stress tensor is also present in the Leslie-Ericksen [12–15] theory when Frank elasticity is included.

In the present paper, which focuses on fundamental implications of spatial inhomogeneities, we simplify the model even further by (i) considering a planar structure tensor ($d = 2$), and (ii) considering a symmetric shear flow between two parallel plates, assuming that variations take place only in the direction perpendicular to the channel axis. The plates are moving opposite to each other with speeds $\pm V$ and are separated by a gap distance H.

We next rewrite the equations in dimensionless form. We measure velocities in units of wall speed V, lengths in units of channel width H, and stresses in units of $c\,k_{\mathrm{B}}T$. This is the correct scaling for the stress if one is interested in the limit of low Reynolds numbers where the fluid density should not play any role. The geometry of the system in dimensionless units is shown in Fig. 1, while the dimensionless equations are given by

$$\left(\frac{\partial}{\partial t} + \boldsymbol{v}\cdot\boldsymbol{\nabla}\right)\boldsymbol{S} = \boldsymbol{F}(\boldsymbol{S}) + \boldsymbol{G}(\boldsymbol{S}), \tag{17}$$

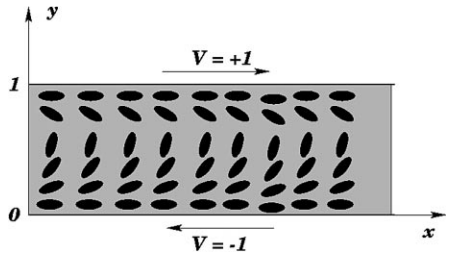

Fig. 1. Schematic illustration of the flow geometry. The channel axis is parallel to the x-axis, with the channel walls coinciding with the planes $y = 0,\ 1$; the top and the bottom walls move at speeds $+1$ and -1, respectively.

$$\boldsymbol{F}(\boldsymbol{S}) = \boldsymbol{F}^{\mathrm{h}}(\boldsymbol{S}) + \boldsymbol{F}^{\mathrm{nh}}(\boldsymbol{S}), \tag{18}$$

$$\boldsymbol{F}^{\mathrm{h}}(\boldsymbol{S}) = \frac{4}{\mathrm{De}}\left[\left(1 - \frac{3}{4}U\right)\boldsymbol{S} - \frac{3}{2}U\boldsymbol{S}\cdot\boldsymbol{S} + \frac{3}{2}U(\boldsymbol{S}:\boldsymbol{S})\left(\boldsymbol{S} + \frac{1}{2}\boldsymbol{\delta}\right)\right], \tag{19}$$

$$\boldsymbol{F}^{\mathrm{nh}}(\boldsymbol{S}) = \frac{1}{\mathrm{Er}}\left\{(\nabla^2\boldsymbol{S})\cdot\boldsymbol{S} + \boldsymbol{S}\cdot(\nabla^2\boldsymbol{S}) + \nabla^2\boldsymbol{S} - 2[(\nabla^2\boldsymbol{S}):\boldsymbol{S}]\left(\boldsymbol{S} + \frac{1}{2}\boldsymbol{\delta}\right)\right\}, \tag{20}$$

$$\boldsymbol{G}(\boldsymbol{S}) = \frac{1}{2}(\boldsymbol{\kappa} + \boldsymbol{\kappa}^{\dagger}) + \boldsymbol{S}\cdot\boldsymbol{\kappa}^{\dagger} + \boldsymbol{\kappa}\cdot\boldsymbol{S} - 2(\boldsymbol{\kappa}:\boldsymbol{S})\left(\boldsymbol{S} + \frac{1}{2}\boldsymbol{\delta}\right), \tag{21}$$

$$\mathrm{Re}\left(\frac{\partial}{\partial t} + \boldsymbol{v}\cdot\boldsymbol{\nabla}\right)\boldsymbol{v} = -\boldsymbol{\nabla}p + \boldsymbol{\nabla}\cdot\boldsymbol{\tau}, \tag{22}$$

$$\boldsymbol{\tau} = -\frac{1}{2}\lambda\mathrm{De}\boldsymbol{F}(\boldsymbol{S}) + \frac{1}{2}\frac{\mathrm{De}}{\mathrm{Er}}[(\nabla^2\boldsymbol{S})\cdot\boldsymbol{S} - \boldsymbol{S}\cdot(\nabla^2\boldsymbol{S})] + \nu_{\mathrm{s}}\boldsymbol{D}, \tag{23}$$

where all quantities have been rescaled appropriately. The equations contain six dimensionless parameters.

The parameters U and λ have already been defined, and represent the dimensionless molecular concentration and the molecular aspect ratio, respectively. The Deborah number,

$$\mathrm{De} = \frac{V}{\bar{D}_{\mathrm{R}}H}, \tag{24}$$

is the ratio between the molecular time scale, $\bar{D}_R^{-1}$, and the mean inverse shear rate, H/V. The Ericksen number,

$$\mathrm{Er} = \frac{8VH}{U\bar{D}_{\mathrm{R}}R^2} = \frac{8}{U}\left(\frac{H}{R}\right)^2\mathrm{De}, \tag{25}$$

characterizes the strength of the short range nematic potential relative to the long range Marrucci–Greco elastic potential. The parameter

$$\nu_{\mathrm{s}} = \frac{\eta_{\mathrm{s}}(V/H)}{ck_{\mathrm{B}}T} \tag{26}$$

is the ratio between the solvent viscosity, η_s, and the characteristic polymeric viscosity; the latter is the ratio between the characteristic stress, $c\,k_B T$, and the shear rate, V/H. Finally, the Reynolds number,

$$\mathrm{Re} = \frac{\rho V^2}{c k_B T} \tag{27}$$

is as usual the ratio between the inertial stress, $\rho\,V^2$, and the other sources of stress, which are of the order of $c\,k_B T$.

Boundary conditions must be prescribed to specify the model completely. For the velocity field, no-slip conditions are assumed, so that the dimensionless velocity equals -1 and $+1$ at the walls, which coincide with the planes $y = 0$ and $y = 1$, respectively. For the structure tensor we assume that the director is aligned with the walls (anchoring walls), with the magnitude of $\boldsymbol{S}$ equal to the equilibrium value obtained for the homogeneous case, namely,

$$\boldsymbol{S}(y = 0, 1) = \begin{pmatrix} S_{eq} & 0 \\ 0 & -S_{eq} \end{pmatrix}, \tag{28}$$

where

$$S_{eq} = \frac{1}{2}\sqrt{1 - \frac{4}{3U}}. \tag{29}$$

3. Computational procedure

Eqs. (17)–(23) were solved numerically using a second-order finite-difference scheme. We notice that the structure tensor, $\boldsymbol{S}$, is driven by the shear rate, which is the first derivative of the shear velocity, $\boldsymbol{v}$, whereas the shear velocity is driven by first derivatives of the stress, which is itself a function of the structure tensor. This suggests the use of a hybrid discretization, where the structure tensor and the shear velocity are discretized on two meshes that are mutually displaced (staggered) by half a mesh size; an illustration of the computational mesh is shown in Fig. 2. The two meshes are defined such that the end points of the mesh used by the velocity field lie on the boundaries, and their values are prescribed by the no-slip boundary conditions.

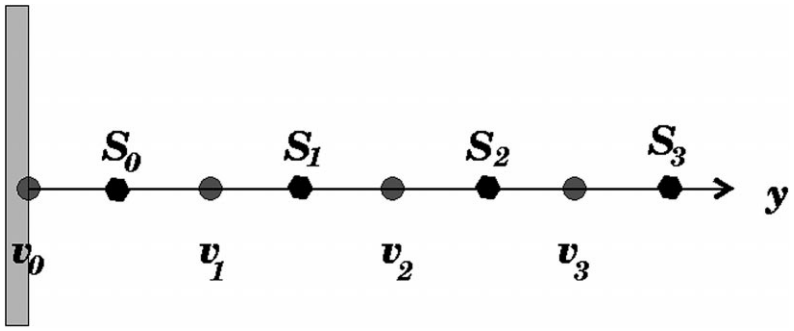

Fig. 2. The computational mesh.

The numerical scheme is constructed using a second-order spatial discretization of the equations of motion, along with a fourth-order Runge–Kutta time integration scheme. The time steps were selected adaptively to satisfy a prescribed error tolerance criterion. The boundary conditions for the structure tensor were imposed by using an appropriate stencil to evaluate the spatial derivatives of $\boldsymbol{S}$ at the end points.

Most computations were performed using $N = 100$ mesh points. In some cases, it proved necessary to obtain a better resolution near the channel walls. Rather than refining the mesh uniformly throughout the channel, we generated a variable distribution of mesh points by reparameterizing the y-coordinate by introducing a computational coordinate, α, with

$$y(\alpha) = \frac{1}{2}\left[1 + \frac{\tanh \delta(\alpha - (1/2))}{\tanh(\delta/2)}\right], \tag{30}$$

where δ is an adjustable parameter of the mapping. We then used a regularly spaced mesh on the α axis, and calculated the spatial derivatives with respect to y by using the transformation rules:

$$\frac{\partial}{\partial y} = \left(\frac{\partial y}{\partial \alpha}\right)^{-1} \frac{\partial}{\partial \alpha}, \quad \frac{\partial^2}{\partial y^2} = \left(\frac{\partial y}{\partial \alpha}\right)^{-2} \left[\frac{\partial^2}{\partial \alpha^2} - \left(\frac{\partial y}{\partial \alpha}\right)^{-1} \frac{\partial^2 y}{\partial \alpha^2} \frac{\partial}{\partial \alpha}\right] \tag{31}$$

Such a mapping allows control of the distribution of points in the $[-1, 1]$ interval, while retaining the second-order accuracy of the spatial discretization.

4. Results and discussion

4.1. Choice of parameters

The model introduced in Section 2 includes six parameters: U, λ, De, Er, Re, and ν_s. U is a dimensionless molecular concentration. We are interested in concentrated solutions, which are typically at least three to four times more concentrated than the critical concentration at the nematic-isotropic transition $U = (4/3)$, so we used values in the range $U = 6 - 10$.

The parameter λ represents the molecular aspect ratio. We choose to work with a fixed value of $\lambda = 0.8$, which corresponds to an aspect ratio of 3, in order to obtain relatively short tumbling periods. An aspect ratio of 10 is probably more reasonable, which would correspond to $\lambda = 0.98$. We verified that larger values of λ caused a slight shift in the onset of the tumbling regime and increased the tumbling period without affecting any of the results qualitatively.

Typical shear rates in experiments are of the order of $1\ s^{-1}$ or less. The diffusion coefficient $\bar{D}_R$, on the other hand, is not precisely defined. We took De to be in the range 0.1 to 10.

The phenomenological parameter R is estimated to be of the order of microns, which is a typical size of a domain in a polydomain morphology. Thus H/R will be large, typically 10^3 or more. The Ericksen number is therefore larger than the Deborah number by at least a factor of 10^6. Such large values of Er lead to very fine spatial structures which require very finely resolved computations. To limit the computational costs we restricted ourselves to smaller values of Er that are still large compared to the Deborah number, corresponding to H/R in the range of 10 to 100.

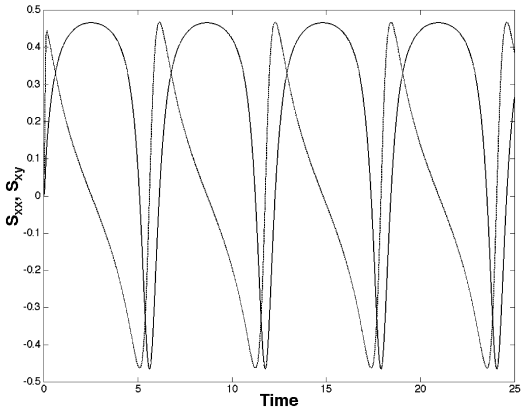

Fig. 3. Evolution of the structure tensor components S_{xx} (solid line) and S_{xy} (dashed line) for the homogeneous point-model in the tumbling regime; the parameters are $U = 10$ and $\mathrm{De} = 1$.

Re was taken equal to 1, which is large relative to the usual value in experiments, but smaller values resulted in little change in behavior while slowing the computations greatly. ν_s should be small for concentrated solutions and melts, and it was set to zero for all computations reported here.

4.2. Homogeneous solutions

We start by studying homogeneous solutions, which are solutions of the 'point-model',

$$\frac{\mathrm{d}\boldsymbol{S}}{\mathrm{d}t} = \boldsymbol{F}^{\mathrm{h}}(\boldsymbol{S}) + \boldsymbol{G}(\boldsymbol{S}), \tag{32}$$

where the shear rate is constant and is equal in our parameterization to $(\partial v_x/\partial y) = 2$. Eq. (32) constitutes a set of two ordinary differential equations for the independent variables S_{xx} and S_{xy} (the 2×2 tensor $\boldsymbol{S}$ is symmetric and traceless).

The nematic-isotropic transition occurs at a critical value of $U = 4/3$. For values of U slightly above the transition, the solutions to Eq. (32) reach a steady-state which is independent of the initial conditions. Although the nematic state has a continuous degeneracy, this symmetry is broken by the shear terms, resulting in a unique steady solution.

For sufficiently large values of U, the system reaches a limit cycle in which the director rotates; this limit cycle is referred to in the literature as the tumbling state. A typical tumbling solution is shown in Fig. 3. In Fig. 4a we show the evolution of the orientation of the director for the same solution; note that the discontinuity of the curve is an artifact of the orientation being defined by an angle in the range $(-\pi, \pi]$; the rotation of the director is continuous.

For sufficiently large values of the Deborah number an intermediate range of U exists, between the steady and the tumbling regimes, where a different limit cycle is attained, in which the director oscillates rather than rotates; this solution is known as 'wagging.' An example of a wagging solution is shown in Fig. 4b.

Finally, we present in Fig. 5 a phase diagram that shows the transition lines in the De–U plane between the three types of solutions. Note that a tumbling transition occurs at a finite value of U even as the

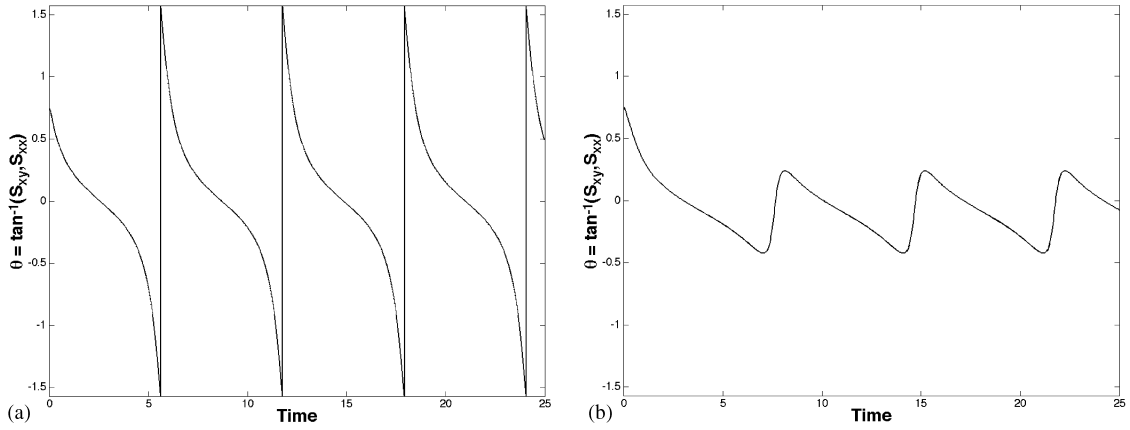

Fig. 4. Evolution of the orientation of the director, $\theta = (1/2)\tan^{-1}(S_{xy}/S_{xx})$, for the homogeneous model. (a) Tumbling for $U = 10$ and $\mathrm{De} = 1$. (b) Wagging for $U = 6$ and $\mathrm{De} = 10$.

Deborah number tends to zero. The behavior in this flow is the same as for the basic Doi model with the inclusion of the finite aspect ratio and quadratic closure, since only the Maier–Saupe contribution to the potential enters into the homogeneous kinetics. The solution to the full Doi model for rods with infinite aspect ratio in shear flow without any closure approximation has been calculated recently by Faraoni and coworkers [16]. Including the finite aspect ratio permits dynamic behavior that is contained in the exact Doi model with an infinite aspect ratio but cannot occur for an infinite aspect ratio with quadratic closure. Rey and Tsuji [4] have found these modes for the 'complete' model, as well as out-of-plane modes that were not sought here.

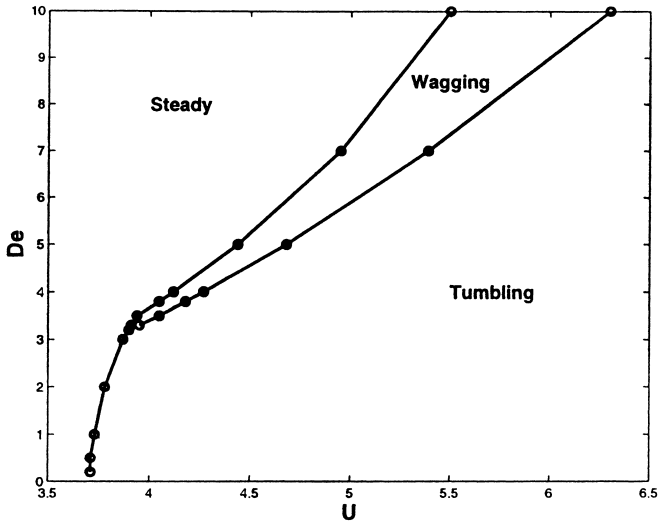

Fig. 5. Diagram of flow regimes as functions of the nematic strength, U, and the Deborah number, De, for the homogeneous model. This section of the parameter space exhibits steady, tumbling, and wagging solutions.

4.3. Inhomogeneous solution: decoupled model

We next add the elastic coupling and the anchoring to the solid walls. These effects have been investigated in the past (e.g., Rey and Tsuji [4]), without accounting for the coupling between the nematic structure and the momentum equation; i.e., the problem that has been considered, and which we consider in this section, is one in which the shear rate is prescribed to remain uniform and constant at all times. We will refer to this model as the 'decoupled' inhomogeneous model. In this case, we have an additional parameter, the Ericksen number, Er; small values of the Ericksen number correspond to strong elastic coupling.

In Fig. 6 we show surface plots that represent the time evolution of the functions $S_{xx}(y)$, $S_{xy}(y)$, and $|\boldsymbol{S}(y)|$ for $U = 10$, De $= 1$, and Er $= 100$; the values of U and De lie inside the tumbling regime for the homogeneous equations. These results are generic: far enough from the walls, the structure tensor behaves very similarly to its behavior in the homogeneous case (cf. Fig. 3), and there is a boundary layer that connects the almost-uniformly tumbling region to the anchoring at the wall. Note that during

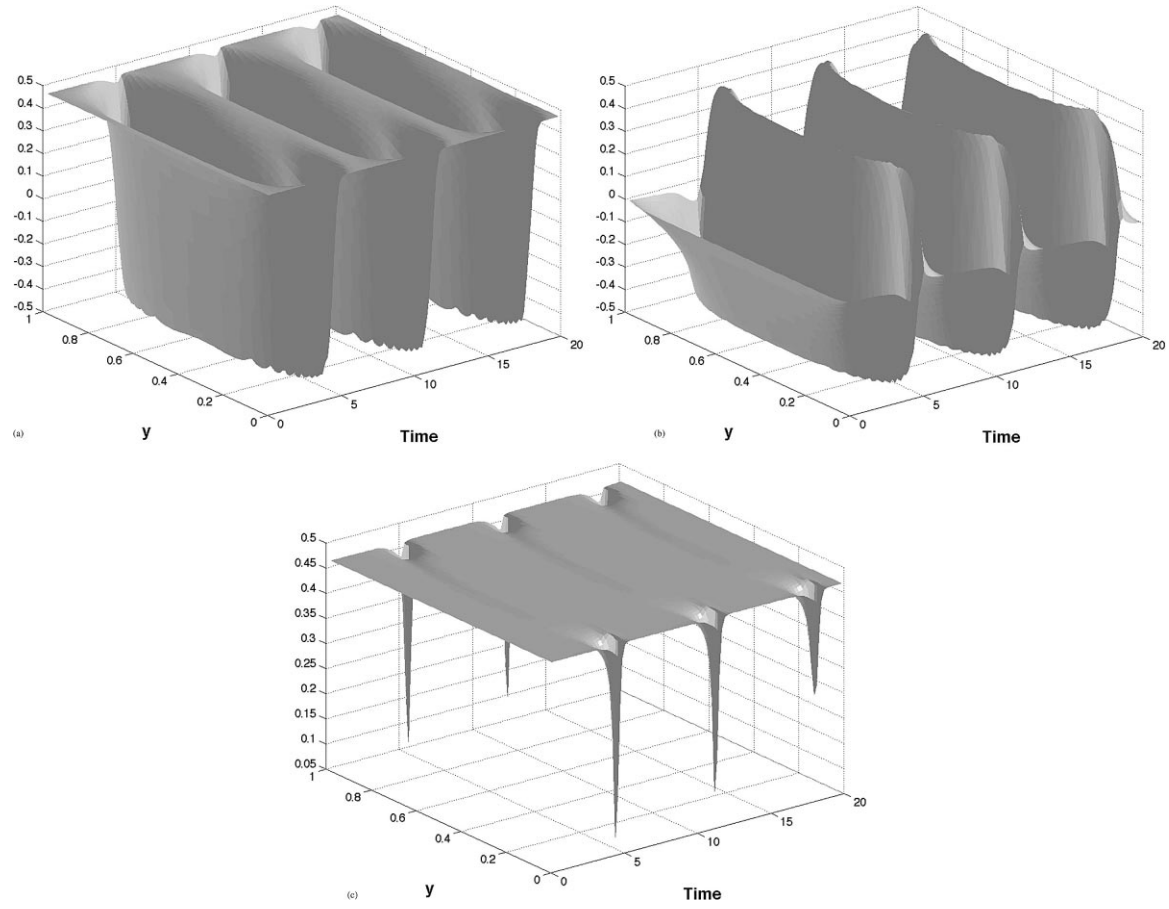

Fig. 6. Surface plots of (a) $S_{xx}(y,t)$, (b) $S_{xy}(y,t)$, and (c) $|\boldsymbol{S}(y,t)|$ for the decoupled model. The parameters are $U = 10$, De $= 1$, and Er $= 100$.

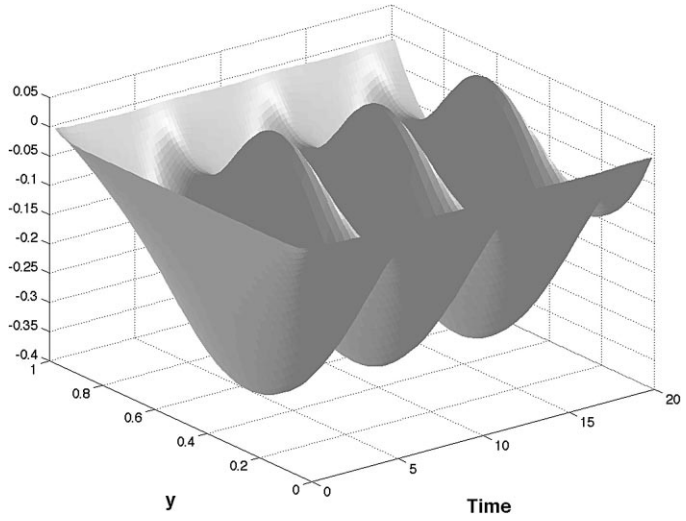

Fig. 7. The orientation field $\theta(y, t)$ for the decoupled model. The parameters are $U = 6$, De $= 10$, and Er $= 100$.

each tumbling cycle, a defect line must form on each side of the central axis. These defects are however smoothly removed without the formation of any singularity. The mechanism of smooth defect removal can be observed in Fig, 6c, which shows that the magnitude of $\boldsymbol{S}$ vanishes periodically in the vicinity of the wall; it is a momentary destruction of the nematic order that allows for a smooth removal of defects, and appears to be equivalent to the 'compatabilization' observed by Rey and Tsuji [4].

In Fig. 7 we show the evolution of the nematic orientation $\theta(y)$ in the wagging regime. Here again, the bulk is governed by the homogeneous dynamics with a boundary layer connecting it to the anchoring at the walls.

4.4. Inhomogeneous solution: full model

We now examine the full model, including the coupling between the nematic structure and the momentum equation. We keep U fixed equal to 10 for all calculations reported in this section, and we consider only the case in which the solvent viscosity is negligible ($\nu_s = 0$), so the dissipation of energy is entirely due to the polymeric viscosity. We set Re $= 1$ for all calculations, and vary De and Er.

A first set of results is shown in Fig. 8 for De $= 0.1$ and Er $= 100$. Naively, one might expect the solution to differ only slightly from the solution in the case of the decoupled model, i.e., to reach a tumbling limit cycle. The outcome is very different from the naive expectation, however, and shows that the coupling to the momentum equation cannot, in general, be treated as a small perturbation. Rather than reaching a limit cycle, the system tends towards a spatially structured steady state. The time-dependent picture shows that the director in the central section of the channel tumbles once before a balance between elastic and shear forces is reached. Note the beginning of a cavity in the profile of S_{xx}, indicating an attempt to tumble once more which was countered by the elastic forces.

Even more surprising is the state approached by the velocity field v_x (Fig. 8b). The asymptotic velocity profile is almost flat throughout most of the channel section, and exhibits very large gradients that are concentrated in the vicinity of the two walls and at the center of the channel. In these three bands, where

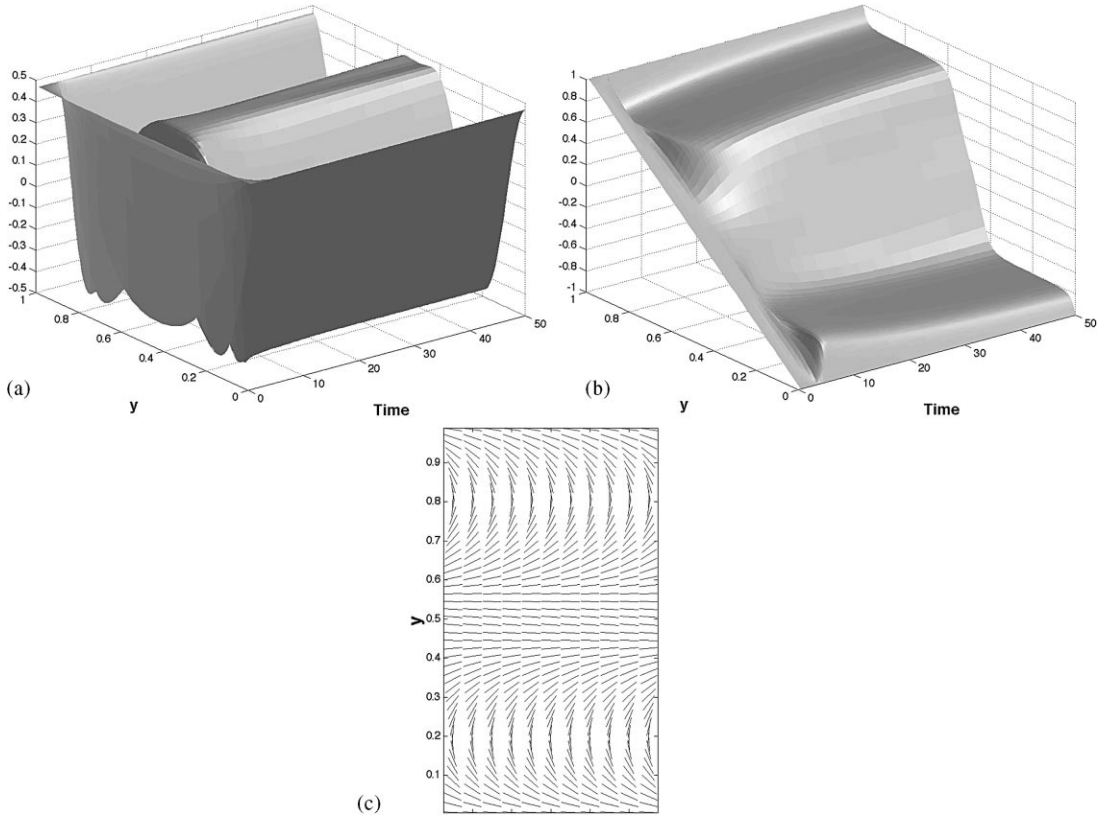

Fig. 8. Simulation results for Re $= 1$, De $= 0.1$, and Er $= 100$: (a) the structure tensor component, $S_{xx}(y, t)$, (b) the shear velocity $v_x(y, t)$, and (c) visualization of the nematic orientation in the steady-state.

the velocity seems to drop discontinuously, the director is parallel to the flow lines; flow alignment of the polymers drastically reduces the local polymer viscosity. Obviously, large velocity gradients are possible, partly due to the absence of solvent viscous forces. (The simulation does not allow us to determine with certainty whether a steady state has in fact been reached, or if the balance between flow and elastic stresses simply introduces a new long time scale. We verified that the state approached by the time-dependent solution is indeed a stationary one by using a nonlinear solver for the time-independent equations.)

In Fig. 9 we present results for Er $= 200$. A larger value of Er implies weaker elastic stresses relative to the flow stresses. As a result, the director in the central section of the channel tumbles twice before a balance is reached. This time, there are five narrow bands (including the vicinity of the walls) in which the director is approximately parallel to the flow lines, giving rise to five narrow bands with very large velocity gradients. A careful analysis of the velocity profile indicates the possibility of jump discontinuities at those points. A discontinuous velocity profile is not a priori forbidden by the equations of motion, which may allow for weak solutions; this issue requires a more elaborate analysis, however.

In Fig. 10 we show velocity profiles for fixed Deborah number and increasing values of the Ericksen number. As expected, the larger the Ericksen number, the larger is the number of defect lines across the channel. In all four cases, the final state attained by the system is close to a stationary solution. An

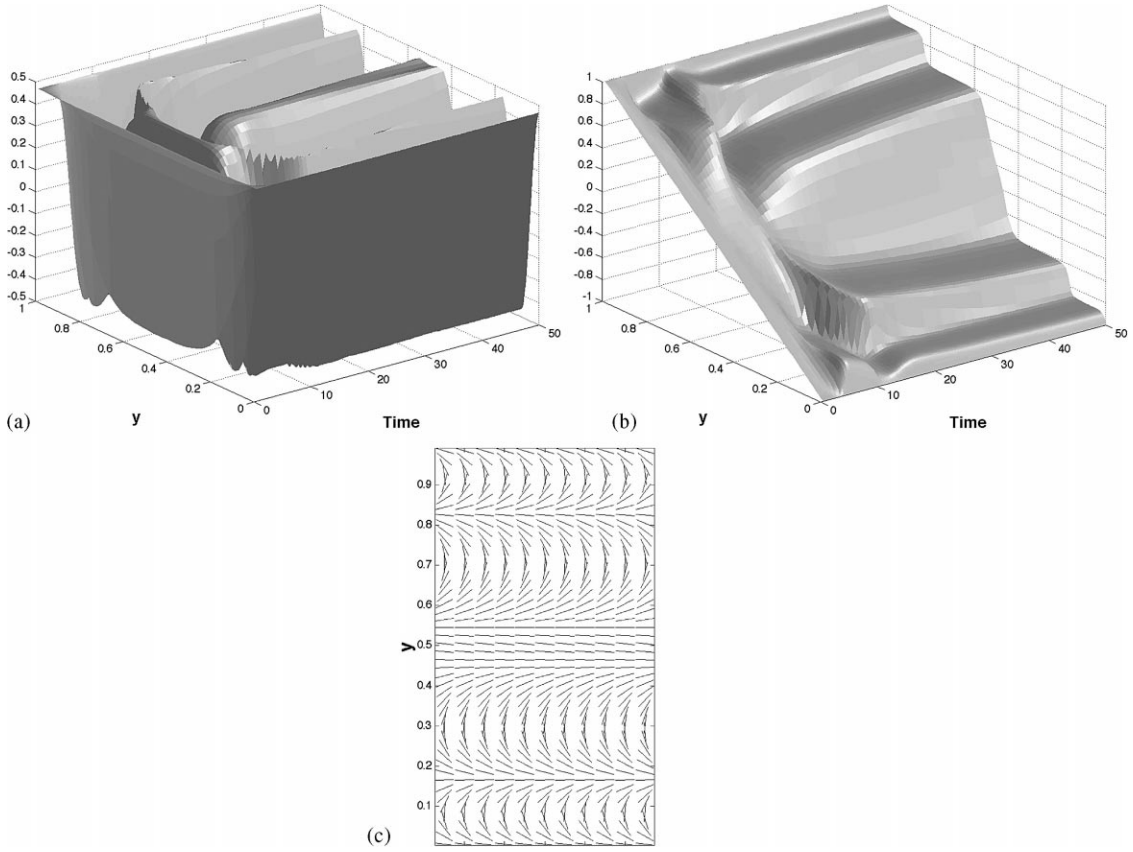

Fig. 9. Simulation results for Re $= 1$, De $= 0.1$, and Er $= 200$: (a) the structure tensor component, $S_{xx}(y,t)$, (b) the shear velocity, $v_x(y,t)$, and (c) visualization of the nematic order in the steady-state.

important observation is that the asymptotic state does not seem to have a characteristic length scale; the distance between defect lines is not fixed, but is shorter the closer they are to the wall. The transverse orientation patterns are in fact reminiscent of those obtained for tumbling nematics described by the Leslie–Ericksen equation [1,17].

The model exhibits a rich range of dynamical behaviors, as can be seen in Fig. 11, where we increased the Deborah number to De $= 1$. For low values of the Ericksen number, the system approaches a steady-state, similar to the one described above. For Er $= 400$, however, the system reaches a spatio-temporally-structured limit cycle. As above, the director in the middle section tumbles, generating smooth orientational waves. Now, however, instead of reaching a stress balance, the outermost defect line is annihilated as it is squeezed between the propagating wave and the anchoring wall. This process repeats periodically, with defect lines generated by director tumbling at the center of the channel and removed near the walls. This defect annihilation is examined with better temporal resolution in Fig. 11c.

The velocity field (Fig. 11b and d), on the other hand, exhibits a truly unusual behavior. The annihilation of the defect line releases a large amount of elastic energy, and is accompanied by a strong torque; this

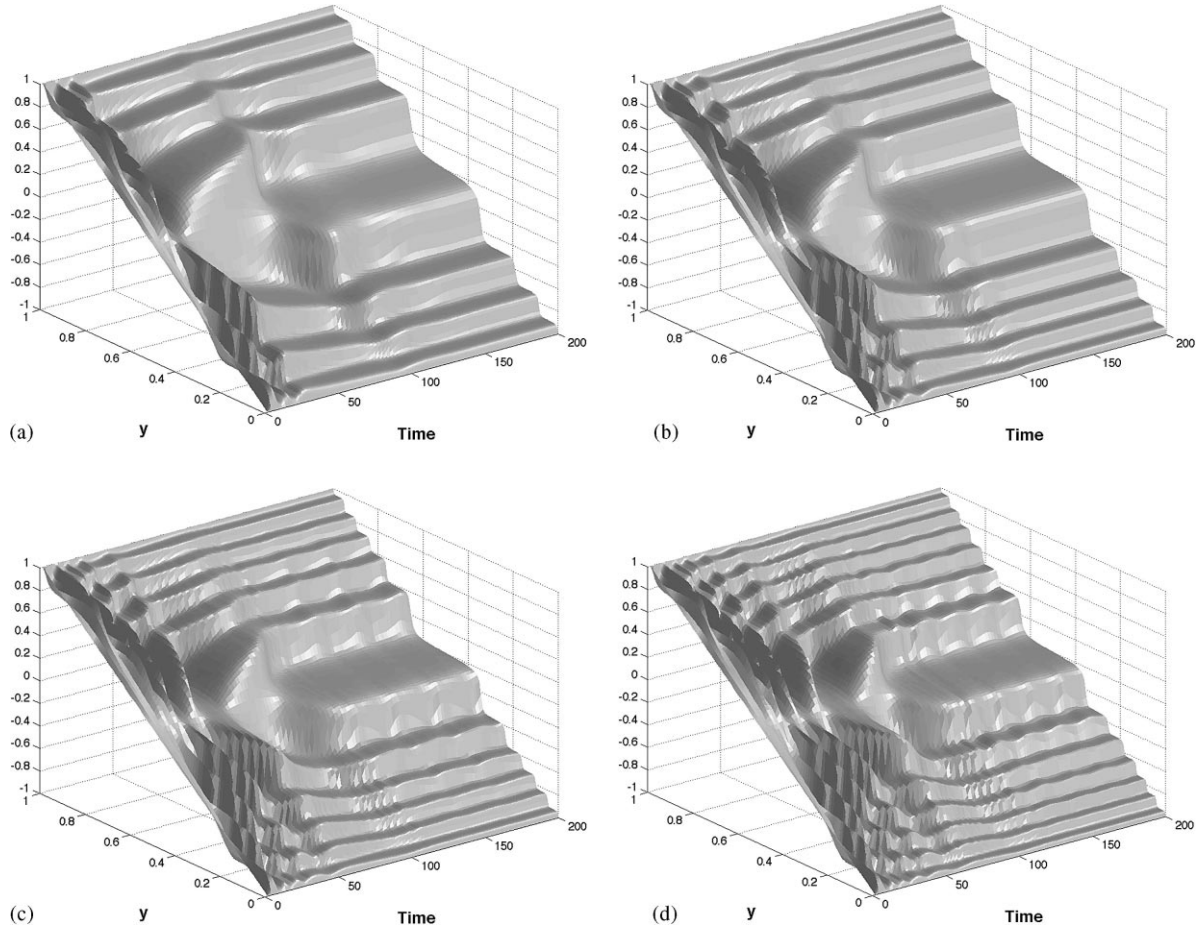

Fig. 10. The velocity profile, $v_x(y,t)$, for De $= 0.1$ and (a) Er $= 300$, (b) Er $= 400$, (c) Er $= 500$, and (d) Er $= 600$.

creates a strong and concentrated vortex. Note that during a short interval of time the maximum velocity inside the channel significantly exceeds the driving wall velocities.

4.5. Length scales

The Marrucci–Greco potential contains a new parameter with dimensions of length, and one might expect to observe the evolution of structures that scale with this length instead of the global length, H. Let ℓ denote any length scale of the solution that does not depend on the global geometry; i.e., is insensitive to the width of the channel, H. Generally, one can write ℓ as a characteristic length scale times a function of all the independent dimensionless groupings of parameters, namely,

$$\ell = R\,\Phi(U, \mathrm{De}, \mathrm{Er}, \lambda), \tag{33}$$

where Φ is a function of its arguments. Because ℓ is assumed independent of the global geometry, its only dependence on H can be through the shear rate, V/H, and as a result cannot be a function of the

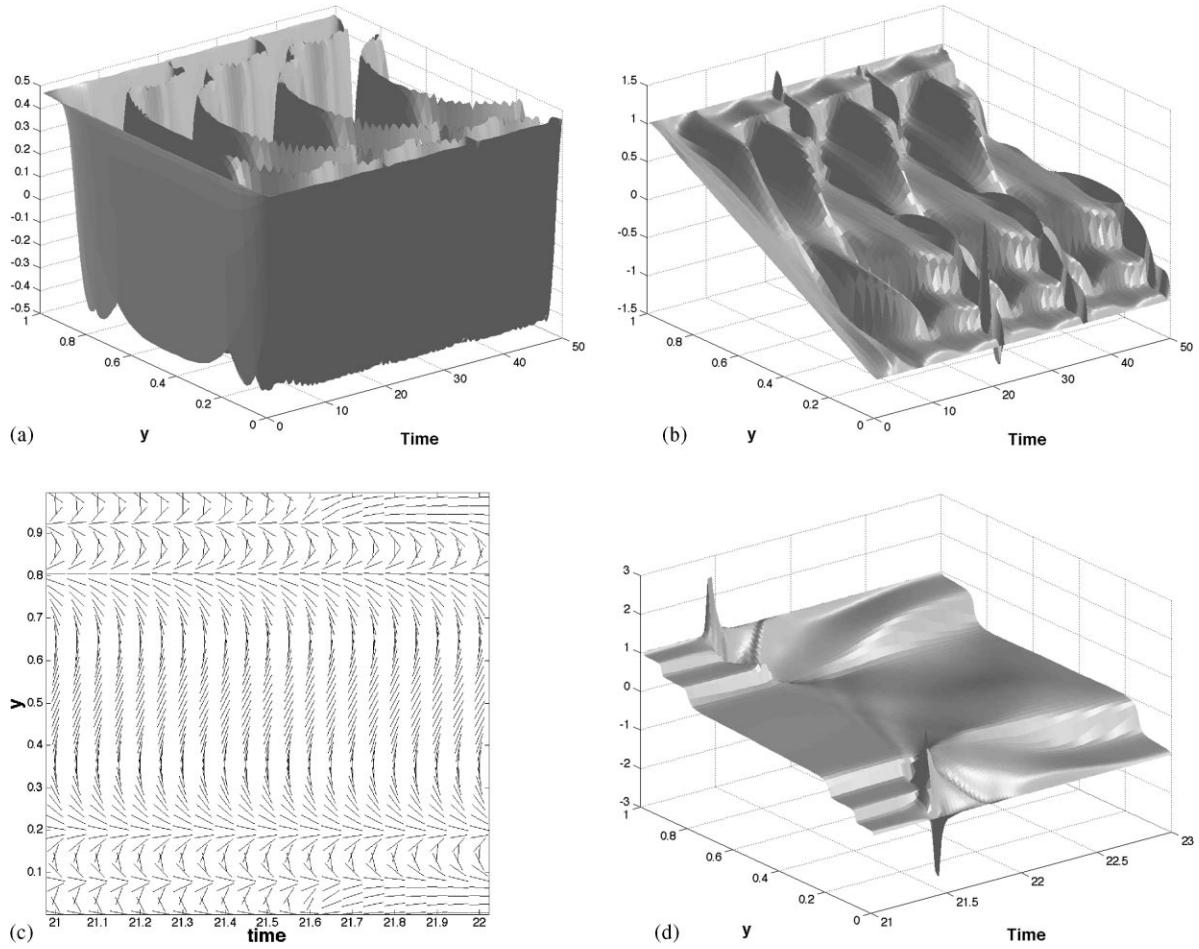

Fig. 11. Simulation results for De = 1 and Er = 400: (a) the structure tensor component $S_{xx}(y,t)$, and (b) the shear velocity $v_x(y,t)$. Figures (c) and (d) show a visualization of the structure tensor and the velocity profile for a magnified time interval $t = [21, 23]$.

Ericksen number. Transforming to dimensionless variables this implies

$$\frac{\ell}{H} = \frac{R}{H}\,\Phi(U, \mathrm{De}, \lambda) = \left(\frac{8\,\mathrm{De}}{U\,\mathrm{Er}}\right)^{1/2} \Phi(U, \mathrm{De}, \lambda) \equiv (\mathrm{Er})^{-1/2}\,\Phi'(U, \mathrm{De}, \lambda). \tag{34}$$

Hence, the width of an orientation layer should scale with the inverse square root of the Ericksen number for fixed De. This observation has direct implications for the numerical procedure. An increase of the Ericksen number by a factor r reduces all (dimensionless) characteristic length scales by a factor of $r^{-1/2}$, and therefore requires a discretization that is finer by a factor of $r^{1/2}$. The simulations shown here do not in fact seem to indicate the development of structures that scale in size with $\mathrm{Er}^{-1/2}$.

5. Conclusions

The inclusion of a Marrucci–Greco potential in a Doi model with finite aspect ratio introduces a rich set of dynamics in simple shear flow, including a remarkable periodic vorticity 'burst' near the shearing surface and very large gradients in velocity at discrete planes. Full coupling of the structure and momentum equations is required to observe the rich dynamics. By analogy to prior studies of the Doi equation (e.g., [16]) and the 'complete' theory of Rey and Tsuji [4], we may assume that some of the textures observed in a two-dimensional simulation are unstable to three-dimensional disturbances, and an even richer range of dynamics is possible for three-dimensional flows.

There is one disappointment in these simulations. The Marrucci–Greco nematic potential was conceived as a means of addressing the role of defects in the flow of liquid-crystalline polymers by introducing a length scale characteristic of molecular interactions. We do not see the development of textures that scale with Er, as required to be independent of the global dimension of the shear cell, so the interesting textures we do observe are probably unrelated to the development of the micron-size 'domains' characteristic of liquid-crystalline polymers.

Acknowledgements

R. Kupferman was supported in part by the LBNL Directed Research and Development Program. M.N. Kawaguchi and M.M. Denn were supported by the Director, Office of Energy Research, Office of Basic Energy Sciences, Materials Science Division of the U.S. Department of Energy under Contract No. DE-AC073-76SF00098.

References

[1] S. Chono, T. Tsuji, M.M. Denn, Spatial development of director orientation of tumbling nematic liquid crystals in pressure-driven flow, J. Non-Newtonian Fluid Mech. 79 (1998) 515–527.
[2] J. Feng, C.V. Chaubal, L.G. Leal, Closure approximations for the Doi theory: which to use in simulating complex flows of liquid-crystalline polymers?, J. Rheol. 42 (1998) 1095–1119.
[3] G. Marrucci, F. Greco, The elastic constants of Maier–Saupe rodlike molecular nematics, Mol. Cryst. Liq. Cryst. 206 (1991) 17–30.
[4] A.D. Rey, T. Tsuji, Recent advances in theoretical liquid crystal rheology, Macromol. Theory Simul. 7 (1998) 623–639.
[5] M. Doi, Molecular dynamics and rheological properties of concentrated solutions of rodlike polymers in isotropic and liquid crystalline phases, J. Polym. Sci. 19 (1981) 229–243.
[6] M. Doi, S.F. Edwards, The Theory of Polymer Dynamics, Clarendon Press, Oxford, 1986.
[7] G.B. Jefferey, The motion of ellipsoidal particles immersed in a viscous fluid, Proc. R. Soc. London Ser. A 102 (1922) 161–179.
[8] G.G. Lipscomb, M.M. Denn, D.U. Hur, D.V. Boger, The flow of fiber suspensions in complex geometries, J. Non-Newtonian Fluid Mech. 26 (1988) 297.
[9] N. Kuzuu, M. Doi, Constitutive equation for nematic liquid crystals under weak velocity gradient derived from a molecular kinetic equation, J. Phys. Soc. Japan 52 (1983) 3486–3494.
[10] N. Kuzuu, M. Doi, Constitutive equation for nematic liquid crystals under weak velocity gradient derived from a molecular kinetic equation II. Leslie coefficients for rodlike polymers, J. Phys. Soc. Japan 53 (1984) 1031–1040.
[11] M.N. Kawaguchi, Flow Visualization and Modeling of Liquid Crystalline Polymers, PhD thesis, University of California, Berkeley, 1998.
[12] J.L. Ericksen, Anisotropic fluids, Arch. Rat. Mech. Anal. 4 (1960) 231–237.

[13] F.M. Leslie, Some constitutive equations for anisotropic fluids, Q. J. Mech. Appl. Math. XIX (1966) 357–370.
[14] J.L. Ericksen, Equilibrium theory of liquid crystals, in: G.H. Brown (Ed.), Advances in Liquid Crystals, Academic Press, New York, 1976, Vol. 2, pp. 233–298.
[15] F.M. Leslie, Theory of flow phenomena in liquid crystals, in: G.H. Brown (Ed.), Advances in Liquid Crystals, Academic Press, New York, 1979, pp. 1–84.
[16] V. Faraoni, M. Grosso, S. Crescitelli, P.L. Maffetonne, The rigid-rod model for nematic polymers: an analysis of the shear flow problem, J. Rheol. 43 (1999) 829–843.
[17] T. Carisson, Theoretical investigation of the shear flow of nematic liquid crystals with the Leslie viscosity $\alpha_3 > 0$: hydrodynamic analogue of first order transitions, Mol. Cryst. Liq. Cryst. 104 (1984) 307–334.